*Manuscript - New Submission

Structural assessment of a whole toroidal sector of the HELIAS 5-B breeding blanket

G. Bongioví[a]*, A. Häußler[a], S. Giambrone[b], I. Catanzaro[b], R. Forte[b], G. Zhou[a], P. A. Di Maio[b] and the W7-X team

[a]*Karlsruhe Institute of Technology (KIT), Institute for Neutron Physics and Reactor Technology (INR), Hermann-von-Helmholtz-Platz 1, 76344 Eggenstein-Leopoldshafen, GERMANY*

[b]*Università degli Studi di Palermo, Viale delle Scienze, Edificio 6, 90128 Palermo, ITALY*

The European roadmap for the realization of fusion energy considers the stellarator line as a possible long-term alternative to a tokamak DEMO. In this context, from the plasma physics standpoint, the most promising option is a five-field period power plant called HELIcal-axis Advanced Stellarator (HELIAS) 5-B. It is a direct extrapolation of the Wendelstein 7-X, the largest stellarator reactor currently in operation. In order to allow the electricity production, the HELIAS 5-B reactor must be endowed with a breeding blanket (BB). Hence, in this paper, the advancements in the HELIAS 5-B BB design are reported. In particular, the structural assessment of a whole BB period, extending along toroidal direction for 72 °, is depicted. A geometric configuration encompassing dummy BB segments has been set up as full blocks without internal details, to verify the feasibility of the proposed BB segmentation strategy for the whole sector. To this end, the displacement field arising under proper steady state loading conditions has been assessed, considering both the Helium Cooled Pebble Bed (HCPB) and Water Cooled Lithium Lead (WCLL) BB concepts. Then, focusing on the HCPB BB concept, a preliminary geometric design of two BB segments, located at the inboard region of a bean shaped ring, has been carried out. In particular, helium manifolds, cooling plates and segment box cooling channels have been designed. These detailed segments have replaced the corresponding dummies in the whole BB sector in order to investigate their structural behavior with realistic boundaries in highly conservative steady state accidental loading conditions. To this end, the stress field arising within the structure of the two segments has been assessed following the RCC-MRx structural design rules. The study has been performed adopting the Finite Element Method and using the Ansys v.19.1 commercial code. The obtained results will be presented and critically discussed.

Keywords: HELIAS, stellarator, breeding blanket, thermomechanics, FEM analysis.

1. Introduction

The European roadmap for the realization of fusion energy [1] aims at producing electricity by fusion around the half of this century. A realistic date is 2050. To this end, the DEMO fusion reactor is being designed, under the umbrella of European Commission, through the EUROfusion consortium. As foreseen by the roadmap, the DEMO reactor will be a large fusion device based on the tokamak concept. At the same time, EUROfusion is promoting researches on a large fusion reactor conceived according to the stellarator concept. The reason of this parallel research line is to have a valid long-term alternative to the tokamak DEMO.

In this context, feasibility studies of a HELIcal-axis Advanced Stellarator (HELIAS) [2] are presently ongoing. The HELIAS machine is a direct extrapolation of the Wendelstein 7-X (W7-X), the largest stellarator reactor currently in operation, built and run by the W7-X team [3], located at the Max Planck IPP-Greifswald.

In particular, in order to allow producing electric power, the HELIAS machine must be endowed with a breeding blanket (BB) system, just like DEMO is. The studies on the HELIAS BB are at a very early stage compared to the DEMO ones and they are focused on the HELIAS 5-B reactor [4], a large 5-fold stellarator reactor conceived to produce electric power.

Preliminary research activities are ongoing at KIT [5]-[9] in order to gather basic results aimed at developing, in a next future, a sound design of a BB for the HELIAS 5-B fusion reactor. In the studies conducted so far, the most representative regions of the HELIAS 5-B BB (namely the so-called triangular and bean shape BB rings and the central rings of a BB half-sector) have been assessed singularly, in order to investigate, with increasing level of detail, the viability of the proposed BB segmentation strategy in those specific regions.

In the present work, a complete displacement assessment of a whole HELIAS 5-B BB sector, extending along toroidal direction for 72 °, is reported. The scope of the work is to assess the proposed segmentation strategy for the whole sector, still focusing on the triangular and bean shape BB rings.

The novelty introduced by this work is that the two most representative rings are assessed within a whole BB sector (i. e., with a realistic geometric boundary). In addition, the proposed segmentation strategy can also be assessed for the other BB rings. To this purpose, attention has been paid to both Helium-Cooled Pebble Bed (HCPB) and Water-Cooled Lithium Lead (WCLL) BB concepts, presently considered for the next conceptual design phase of the DEMO BB. Dummy segments (namely homogenized blocks without internal details) have been used.

author's email: gaetano.bongiovi@kit.edu

In a second phase, focusing only on the HCPB BB concept, a preliminary detailed geometric design of two BB segments located at the inboard region of a bean shaped ring, has been carried out. These detailed segments have replaced the corresponding dummies within the BB sector. Then, the stress field arising under purposely set-up steady state accidental loading conditions, inferred from DEMO BB loads specification [10] and analysis, has been calculated. Afterwards, the obtained results have been compared against the RCC-MRx structural design rules, in order to assess the structural performances of the proposed geometric configuration for the considered BB segments.

The study has been carried out adopting a numerical approach based on the Finite Element Method (FEM) and using the commercial Ansys v.19.1 FEM code. The adopted methodology, the assumptions, the models set-up and the most significant results are herein reported and critically discussed.

2. The HELIAS 5-B breeding blanket sector

A 3D geometric model of a whole HELIAS-5B BB sector, including dummy Vacuum Vessel (VV) and BB segments (full homogenized blocks without internal details), has been considered (Fig. 1) for the purposes of this study. It extends for 72 ° along the toroidal direction. In detail, it encompasses 16 BB rings, numbered as indicated in Fig. 1. It has to be noted that the BB ring numbering is only defined to point at each BB ring easily. In this context, the BB ring having a triangular shape section is labelled as Ring 5, whereas the BB ring characterized by a bean shape section is the Ring 12.

The 16 BB rings have been designed to be separated by 20 mm gaps along toroidal direction. Each ring is composed by 5 BB segments [11] separated, in their turn, by 20 mm gaps along poloidal direction.

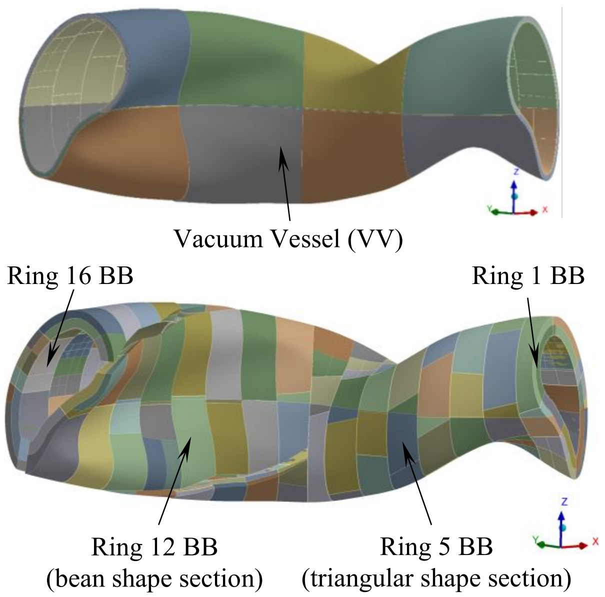

Fig. 1. The HELIAS 5-B BB sector and its VV.

The VV is divided, in its turn, in inner, shield and outer VV, Within each BB segment, the Back Supporting Structure (BSS), the Breeding Zone (BZ), the First Wall (FW) and the 2 mm-thick tungsten armor (W) can be recognized. In Fig. 2, details of Ring 5 and Ring 12 are reported as an example. In this figure, the segments numbering adopted for these two rings is shown as well. A similar approach has been adopted also for the segments numbering of the other BB rings, here not reported for the sake of brevity.

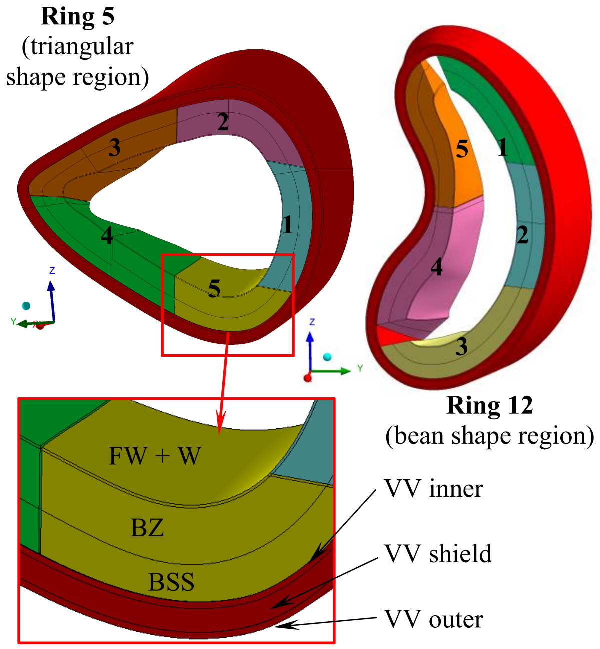

Fig. 2. BB components - details of Ring 5 and Ring 12.

As already presented in [7] and [8], the dummy components representing FWs, BZs and BSSs of Ring 5 and Ring 12 have been purposely sliced by means of a dedicated geometry editing campaign, so to have the possibility to apply a 3D discrete temperature profile. As an example, the sliced Ring 5 is shown in Fig. 3 where a detail of a sliced FW is given as well.

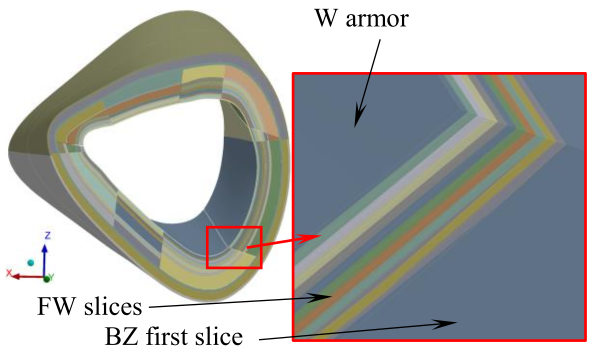

Fig. 3. Ring 5 with sliced components - detail of the FW.

3. Displacement assessment of a whole sector of the HELIAS 5-B BB

The first part of the work reported in this paper is devoted to investigate the displacement field of a whole sector of the HELIAS 5-B BB under the selected loading scenarios. The aim of the work is assessing the proposed segmentation strategy for the whole sector, still putting the focus on the triangular and bean shape rings, i .e Ring 5 and Ring 12 BB.

3.1 The FEM model

The developed FEM model is described in this section, with the focus on the loading scenarios set-up.

3.1.1 Materials and equivalent properties

Concerning structural materials, the RAFM Eurofer steel has been considered for BB whereas AISI 316L steel has been taken into account for the VV. Temperature-dependent thermomechanical properties have been adopted for all the materials, included the W armour covering the FW.

As homogenized dummy segments are considered, equivalent densities have been calculated, for both HCPB and WCLL BB concept, and adopted in order to take the masses of the structural materials, breeder and coolant into account. To this purpose, the same material compositions [12] as the Helium-Cooled Pebble Bed [13]-[15] and Water-Cooled Lithium Lead [16]-[18] DEMO BB concepts have been assumed. In particular, once given the i-th material having a temperature-dependent density ρ_i (T) and once known its volume percentage V_i / V_{tot}, the temperature-dependent equivalent density ρ_{eq} (T) can be calculated by Eq. 1:

$$\boldsymbol{\rho_{eq}(T)} = \frac{\sum_i \boldsymbol{\rho_i}(\mathbf{T}) \cdot \boldsymbol{V_i}}{\boldsymbol{V_{tot}}} \qquad \text{Eq. 1}$$

For the purposes of this study, the other two BB concepts presently considered in Europe for the DEMO studies, namely the Helium-Cooled Lithium Lead [19] and the Dual-Coolant Lithium Lead [20] BB, have not been taken into account as they will not be brought to the next DEMO conceptual phase.

In addition, as dummy segments are still considered in this phase, the same limit values of the equivalent Young's Modulus [21] carried out from [7] and [8] have been kept. Therefore, two limit scenarios can be defined:

- Less Conservative (LC) scenario: that one where E=10% of the actual ones are assumed for structural materials in dummy components (BB segments and VV shield).
- More Conservative (MC) scenario: that one where actual E values are assumed for structural materials in dummy components (BB segments and VV shield).

3.1.2 The spatial discretization grid

As far as the spatial discretization grid is concerned, the "sliced" Ring 5 and Ring 12 have been meshed using linear tetrahedral elements with an average element size of 0.05 m, as already done in in [7] and [8]. The mesh features for these two rings are reported in Table 1.

Table 1. Mesh features for Ring 5 and Ring 12.

Ring	Node number	Element number
5	~0.83M	~2.94M
12	~1.07M	~3.71M

Regarding the rest of the BB sector (i. e. the remaining 14 BB rings plus the VV), a mesh independence assessment has been performed in order to find out a spatial discretization grid with a minimum impact on the results of Ring 5 and Ring 12, allowing to ensure reliable results in a reasonable time. Average element size of 0.05 m, 0.075 m, 0.1 m and 0.2 m have been considered, allowing to generate meshes (adopting linear tetrahedral element) with node number ranging from ~10.8M to ~392k and a corresponding element number ranging from ~52.3M to ~1.3M. The mesh independence assessment, here not detailed for the sake of brevity, has allowed selecting a mesh characterized by ~1.75M nodes connected in ~7.15M linear tetrahedral elements, obtained setting an average element size of 0.1 m. Such a kind of mesh weakly affects the displacement of the detailed Ring 5 and Ring 12.

Hence, in total, the mesh set-up for the whole HELIAS 5-B BB sector presents ~3.65M nodes and ~13.80M elements.

3.1.3 The assumed thermal loads

Concerning the assumed temperature field, the following assumptions have been made on the basis of the results obtained so far from the DEMO BB studies.

As to VV, its three regions (inner, shield and outer) have been assumed at different temperatures. In particular, due to recent indications coming from DEMO VV design, two different cases have been considered:

- Hot VV case [22]: characterized by VV outer at 180 °C, VV shield at 205 °C and VV inner at 230 °C.
- Cold VV case [23]: characterized by VV outer at 40 °C, VV shield at 65 °C and VV inner at 90 °C.

Hence, the following four steady state loading scenarios have been set-up [7][8]:

- LC+Hot VV (E =10%, VV between 180 and 230 °C)
- MC+Hot VV (E =100%, VV between 180 and 230°C)
- LC+Cold VV (E =10%, VV between 40 and 90 °C)
- MC+Cold VV (E =100%, VV between 40 and 90 °C)

In each scenario, the BB thermal state has been assumed as follows, imposing temperatures inferred from DEMO BB thermal analysis [24]-[28].

As to the "sliced" Ring 5 and Ring 12, 3D discrete temperature profiles have been adopted. This means that properly calculated average temperatures have been imposed to each FW, BZ and BSS slice instead of to the full component. As an example, the assumed FW temperature profile is reported in Fig. 4 for both HCPB and WCLL BB concepts.

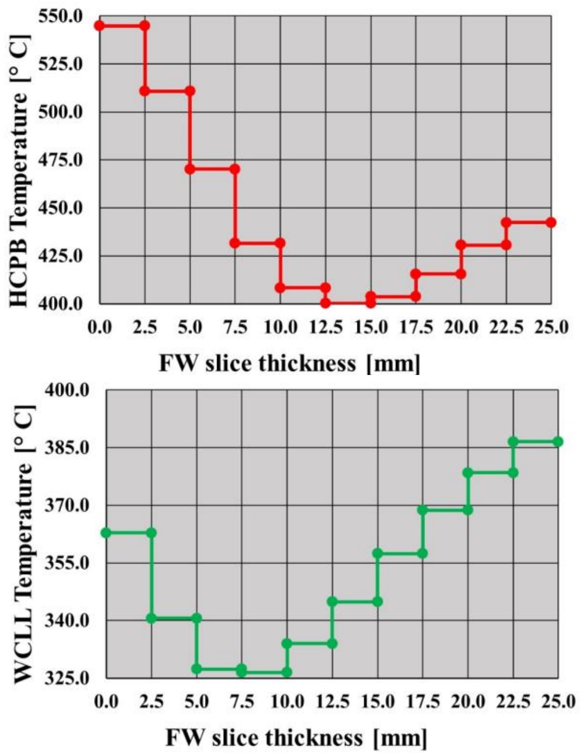

Fig. 4. Discrete 3D temperature distribution assumed within FWs of Ring 5 and Ring 12.

In this regard, the FWs of the two rings have been divided in 10 slices 2.5 mm-thick each and a proper temperature has been assigned to each of them. In particular, the initial FW slice (0-2.5 mm interval in Fig. 4) is that located just behind the tungsten armour. Since the FW is 25 mm thick in all the segments of Ring 5 and Ring 12, the same temperature profile has been imposed to all of them. This is not valid for BZs and BSSs due to the different thicknesses between the segments. This means that varying temperature profiles have been calculated, based on the geometry features, and applied to sliced BZs and BSSs.

Lastly, regarding W armour, 551.4 °C has been assumed for HCPB BB whereas 380 °C have been considered for WCLL BB.

Concerning the remaining 14 "not sliced" rings, proper spatially averaged temperatures, reported in Table 2, have been imposed to every FW, BZ and BSS.

Table 2. Temperatures assumed for the "not sliced" rings.

	HCPB [°C]	WCLL [°C]
W	551.4	380.0
FW	445.8	352.7
BZ	588.0	444.0
BSS	328.5	327.1

3.1.4 The mechanical restraints and gravity load

As a whole BB sector is here assessed, nodes laying onto the far end VV lateral faces (highlighted in red in the upper wireframe view of Fig. 5) have been constrained along the local toroidal direction (namely along the normal direction to each section). This sort of skate condition drives the expansion of the VV onto the radial-toroidal plane. In addition, displacement along the vertical direction has been prevented to nodes laying on the central edges of the VV (highlighted in red in the lower wireframe view of Fig. 5) to simulate a vertical constraint.

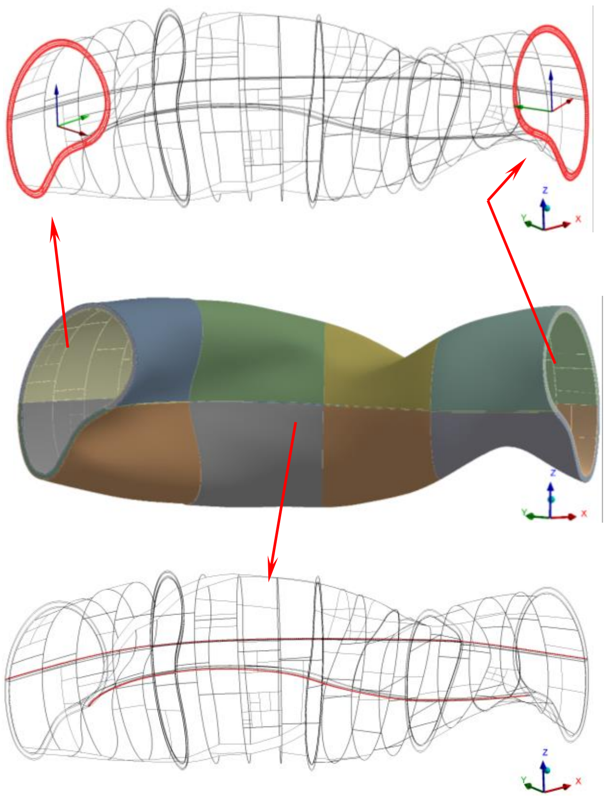

Fig. 5. The adopted mechanical restraints.

Lastly, gravity load has been taken into account considering the global Z direction as the vertical one.

3.2 Results

Under the four selected steady state loading scenarios (LC+Hot VV, MC+Hot VV, LC+Cold VV and MC+Cold VV, called in brief LCH, MCH, LCC and MCC, respectively), thermo-mechanical analyses have been performed in order to carry out the displacement field for the HELIAS 5-B HACPB and WCLL BB.

The minimum residual gaps in between segments (i. e. along poloidal direction) and in between adjacent rings (i. e. along toroidal direction) has been checked. Since the most representative regions are Ring 5 (triangular shape section) and Ring 12 (bean shape section), results concerning these two rings, in terms of both poloidal and toroidal minimum residual gaps, are reported in this section. The complete set of results, concerning all the remaining BB rings, is instead reported in the Appendix. This complete set of results is useful to take a global overview of the response of the BB sector in terms of deformation.

Results in terms of minimum residual gaps along the poloidal direction are shown in Table 3 and Table 4 for Ring 5 and in Table 6 and Table 7 for Ring 12. Within the tables, negative values (in red) mean that overlapping occurs, whereas those values lower than 5 mm (assumed as the lowest desirable minimum residual gap to cope with tolerances) are reported in blue. Furthermore, in these tables, the columns "Δ" represent the variation in the minimum residual poloidal gap passing from cold to hot VV conditions. The adopted color code is: green percentages mean an increasing, red percentages mean decreasing in minimum residual poloidal gap when VV temperatures increase.

Moreover, in Table 5 and Table 8, the influence of the E value in case of Hot VV is summarized. Here, the columns "Δ" represent the variation in the minimum residual poloidal gap going from LC to MC conditions.

Table 3. Ring 5 results - LC scenarios (E=10%).

Minimum residual poloidal gap						
	HCPB [mm]		WCLL [mm]		$\Delta_{LCC-LCH}$%	
Segment	LCC	LCH	LCC	LCH	HCPB	WCLL
1-2	2.6	9.9	9.7	16.0	280	65
2-3	-4.7	5.7	3.4	13.9	221	309
3-4	7.3	12.6	10.7	16.0	73	50
4-5	-5.1	4.9	3.5	13.6	196	289
5-1	4.7	11.1	10.3	16.4	136	59

Table 4. Ring 5 results - MC scenarios (E=100%).

Minimum residual poloidal gap						
	HCPB [mm]		WCLL [mm]		$\Delta_{MCC-MCH}$%	
Segment	MCC	MCH	MCC	MCH	HCPB	WCLL
1-2	5.6	10.1	12.5	16.6	80	33
2-3	-3.2	4.7	5.9	13.9	247	136
3-4	9.1	12.9	12.7	16.3	42	28
4-5	-3.5	4.1	6.0	13.7	217	128
5-1	7.3	11.5	12.6	16.6	58	32

The results reported above clearly show that, in both LC and MC scenarios, the cold VV seems to act like a rigid wall towards BB and overlapping occurs in some gaps for HCPB BB. Indeed, due its low temperature, the cold VV does not accommodate the BB segments thermal expansion. Thus, BB can only move towards the plasma chamber occupying the available space, and this effect results in a significant reduction of the gaps between adjacent rings, somewhere causing overlapping or narrow (i .e. lower than 5 mm) residual gaps. On the contrary, Hot VV cases show better results since the higher VV temperatures allow a greater thermal expansion and the accommodation of the BB strain.

Then, looking at the third column of the tables, the huge percentage variation of the minimum residual poloidal gaps due to the increase in VV temperature is reported to quantify this aspect.

Table 5. Ring 5 results - Hot VV cases.

Minimum residual poloidal gap						
	HCPB [mm]		WCLL [mm]		$\Delta_{LCH-MCH}$%	
Segment	LCH	MCH	LCH	MCH	HCPB	WCLL
1-2	9.9	10.1	16.0	16.6	2	4
2-3	5.7	4.7	13.9	13.9	18	0
3-4	12.6	12.9	16.0	16.3	2	2
4-5	4.9	4.1	13.6	13.7	16	1
5-1	11.1	11.5	16.4	16.6	4	1

Differently from results reported in [8], a moderate influence of the E value on the minimum residual poloidal gap is predicted in case of Hot VV conditions. This is mainly due to the simulation of the whole BB sector, currently assessed rather than a single BB ring, which allow moving the imposed boundary conditions far away from the domain of interest.

Table 6. Ring 12 results - LC scenarios (E=10%).

Minimum residual poloidal gap]						
	HCPB [mm]		WCLL [mm]		$\Delta_{LCC-LCH}$%	
Segment	LCC	LCH	LCC	LCH	HCPB	WCLL
1-2	-4.9	5.5	3.7	14.2	212	284
2-3	-6.2	4.7	2.6	13.5	176	419
4-5	0.5	8.6	7.4	15.6	1620	111

Table 7. Ring 12 results - MC scenarios (E=100%).

Minimum residual poloidal gap						
	HCPB [mm]		WCLL [mm]		$\Delta_{MCC-MCH}$%	
Segment	MCC	MCH	MCC	MCH	HCPB	WCLL
1-2	-3.6	4.3	6.2	14.0	219	126
2-3	-5.3	3.2	4.8	13.3	160	177
4-5	0.1	7.3	8.1	15.2	7200	88

Table 8. Ring 12 results - Hot VV cases.

Minimum residual poloidal gap						
	HCPB [mm]		WCLL [mm]		$\Delta_{LCH-MCH}$%	
Segment	LCH	MCH	LCH	MCH	HCPB	WCLL
1-2	5.5	4.3	14.2	14.0	-22	-1
2-3	4.7	3.2	13.5	13.3	-32	-1
4-5	8.6	7.3	15.6	15.2	-15	-3

Also for Ring 12, the same conclusions obtained for Ring 5 can be deduced. Indeed, comparing results with [8], the effect of the change in E value in case of Hot VV is lower also for this ring. This confirms that the simulation of the whole BB sector allow considerably reducing the effect of the imposed boundary conditions adopted in the previous studies, where single self-standing rings were assessed.

In Fig. 6, the total displacement field predicted for Ring 5 HCPB BB in MCH scenario is depicted. Here, in the detailed pictures, the minimum residual poloidal gaps between segments 2-3 and 4-5 are shown, with the deformed view superimposed to the wireframe undeformed view. In addition, the total displacement field predicted for Ring 12 HCPB BB in MCH scenario is depicted in the same way in Fig. 7, with the focus on segments 1-2 and 2-3 gaps.

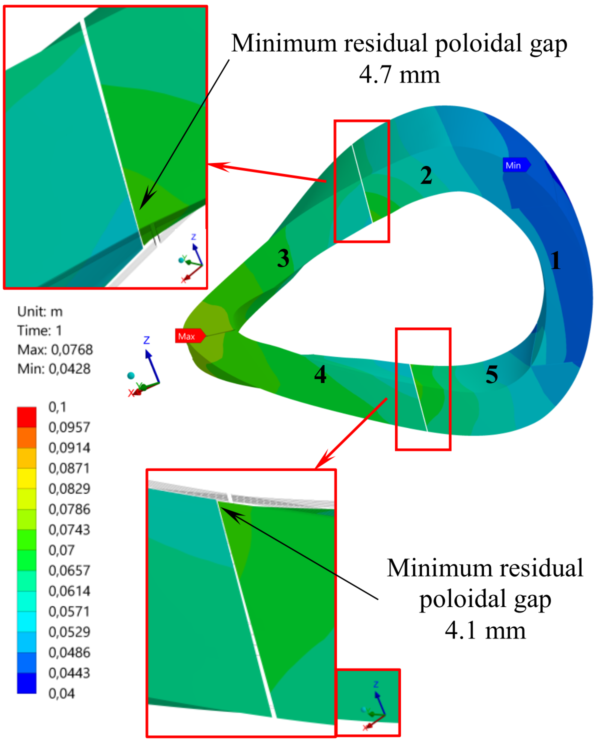

Fig. 6. Displacement for Ring 5 HCPB BB in MCH scenario.

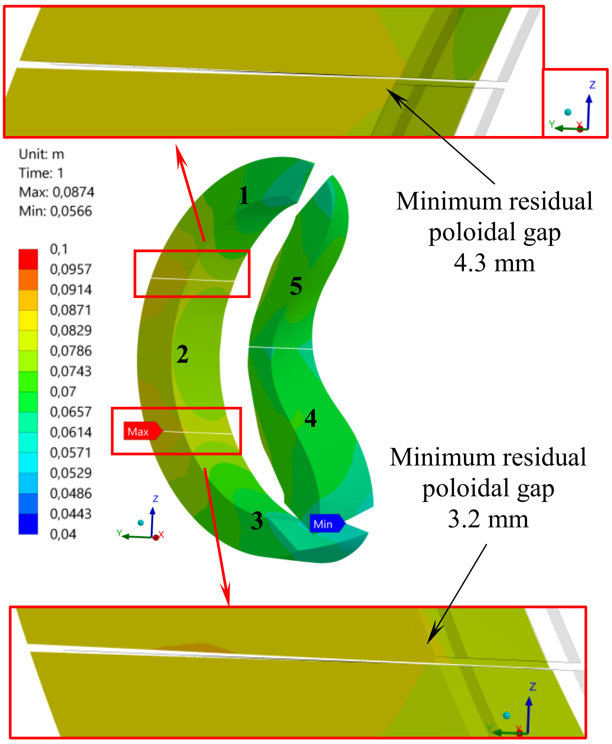

Fig. 7. Displacement for Ring 12 HCPB BB in MCH scenario.

Moreover, as the whole sector has been assessed, the potential overlapping along toroidal direction can be investigated in the present work too. Hence, results in terms of minimum residual gaps along the toroidal direction are shown in Table 9 and in Table 10. Then, in Table 11, the influence of the E value in case of Hot VV is summarized.

Table 9. Ring 5 and Ring 12 results - LC scenarios (E=10%).

	Minimum residual toroidal gap					
	HCPB [mm]		WCLL [mm]		$\Delta_{LCC-LCH}$%	
Rings	LCC	LCH	LCC	LCH	HCPB	WCLL
4-5	4.6	10.4	10.7	16.3	126	52
5-6	2.1	8.9	9.1	15.9	324	75
11-12	7.0	12.0	11.5	16.7	71	45
12-13	6.9	12.2	11.3	16.5	77	46

Table 10. Ring 5 and Ring 12 results - MC scenarios (E=100%).

	Minimum residual toroidal gap					
	HCPB [mm]		WCLL [mm]		$\Delta_{MCC-MCH}$%	
Rings	MCC	MCH	MCC	MCH	HCPB	WCLL
4-5	5.2	10.0	11.6	16.3	92	41
5-6	2.8	8.4	10.3	15.7	200	52
11-12	8.1	12.3	12.7	16.1	52	27
12-13	7.7	12.2	12.1	16.6	58	37

Table 11. Ring 5 and Ring 12 results - Hot VV cases.

	Minimum residual toroidal gap					
	HCPB [mm]		WCLL [mm]		$\Delta_{LCH-MCH}$%	
Rings	LCH	MCH	LCH	MCH	HCPB	WCLL
4-5	10.4	10.0	16.3	16.3	-4	0
5-6	8.9	8.4	15.9	15.7	-6	-1
11-12	12.0	12.3	16.7	16.1	3	-4
12-13	12.2	12.2	16.5	16.6	0	1

As well as already seen along poloidal direction, also for minimum residual toroidal gaps, a moderate influence of the E value is predicted in case of Hot VV conditions. Moreover, toroidal overlapping can be excluded also in case of Cold VV conditions.

Hence, the presented results (see also the complete set of results reported in Appendix) allow concluding that, assuming Hot VV conditions, both poloidal and toroidal overlapping can be excluded with a reasonable margin of confidence. Narrow minimum residual gaps (i. e. values lower than 5 mm) are still predicted, but they may be overcome with a detailed design activity which possibly involves the design of a proper attachment system. In case of Cold VV, the future attachments devoted to connect mechanically the VV to the BB should be able to compensate the high difference in thermal expansion between the two systems.

In conclusion, the predicted total displacement field for the whole HELIAS 5-B BB sector under MCH scenario is depicted in Fig. 8, for both HCPB and WCLL BB concepts.

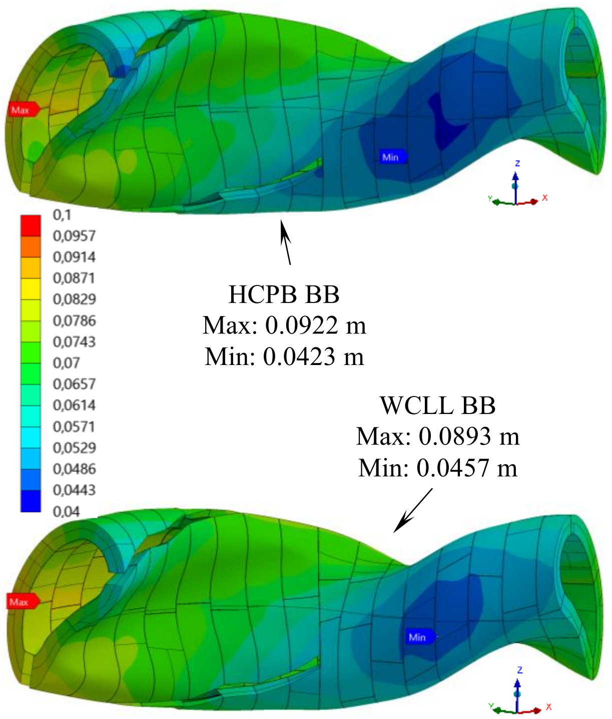

Fig. 8. Displacement field [m] for the whole BB sector in the MC+Hot VV scenario.

4. Stress assessment of the inboard segments of a bean shape ring of the HELIAS 5-B BB

In the second part of the work, a preliminary design of the Ring 12 inboard segments is proposed, focusing on the HCPB BB concept. The so designed segments have replaced the corresponding dummies within the HELIAS 5-B BB sector. Structural analysis under the accidental over-pressurization conditions have been performed, with the aim of investigating the segments structural behaviour. The calculated stress has been compared with the RCC-MRx structural design criteria, highlighting the most critical regions.

4.1 The geometric design

Regardless of the adopted BB concept, the presence of stiffening plates within the BB is essential to ensure the mechanical tightness of the BB structure, especially in accidental loading conditions [13][29]. The design proposed and assessed in this work is based on the “sandwich” architecture developed for the DEMO HCPB BB [13]. In particular, a preliminary design of Segment 4 and Segment 5 (Fig. 2) of Ring 12 has been developed, using the space reservation foreseen in the HELIAS 5-B BB segmentation.

An actively-cooled Segment Box (SB), composed by a First Wall (FW), two Side Walls (SWs), Top and Bottom Cap (TC and BC respectively) has been designed for both Segment 4 (Fig. 9) and Segment 5, trying to mimic as close as possible the square cooling channels (12.5 mm side) of the DEMO HCPB BB “sandwich” SB. The SB is 25 mm thick and it is equipped with a 2 mm-thick tungsten layer that covers only the FW. The SB cooling channels follow the SW-FW-SW path, allowing the heat removal from the whole SB. As shown in [13], the SB cooling channels’ poloidal pitch is equal to 17 mm. In order to try adapting this geometric feature to HELIAS 5-B BB, three main edges (main curvatures) have been selected for both Segment 4 (Fig. 9) and Segment 5. Along these curvilinear edges, points have been picked every 12.5 and 4.5 mm alternately, to reproduce the DEMO SB channels poloidal pitch. Repeating this operation along the three main edges per segment, planes passing through these triplets of points have been drafted and it has been assumed that channels upper and lower faces would lie on them. According to HCPB BB “sandwich” architecture, a 3 mm-thick Eurofer layer separates the SB cooling channels from the plasma facing surface.

Following the same methodology, actively cooled stiffening plates, called Cooling Plates (CPs), have been designed (Fig. 10). They are 5 mm-thick plates endowed with rectangular-shape straight channels (5x2.5 mm cross section), parallel to the FW cooling channels. The CPs spatial arrangement allows leaving space for Be and Li_4SiO_4 beds, foreseeing different poloidal pitches [13]. The same approach as FW channels design has been adopted to derive planes representing the CPs upper and lower faces. Then, cooling channels have been designed within each plate, trying to keep the radial pitch of 7 mm foreseen in the DEMO “sandwich” HCPB BB (Fig. 10) and try to mimic their characteristic to be parallel to FW cooling channels.

In the end, BSS manifolds and Caps cooling channels have been designed too (Fig. 10), trying to keep the same geometric features reported in [13]. The Caps are 84 mm thick. Regarding their cooling channels (square cross section with 36 mm side), a path similar to that of SB channels has been chosen in order to allow the cooling of the component and to contribute to the heat removal from far end regions of the SB.

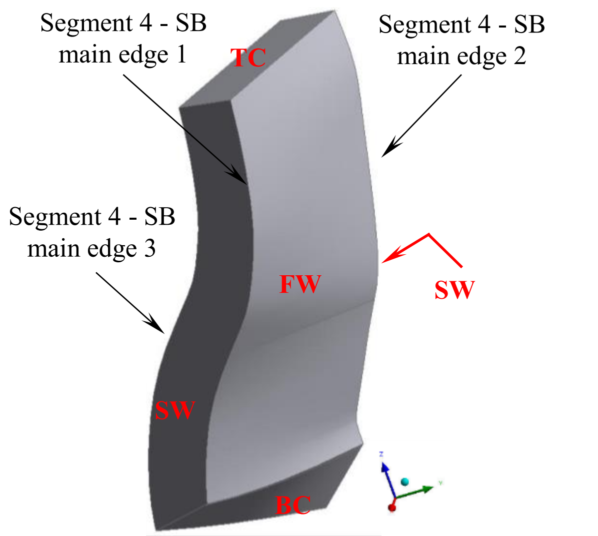

Fig. 9. Ring 12 segment 4: segment box components and main edges for FW channels and CPs design.

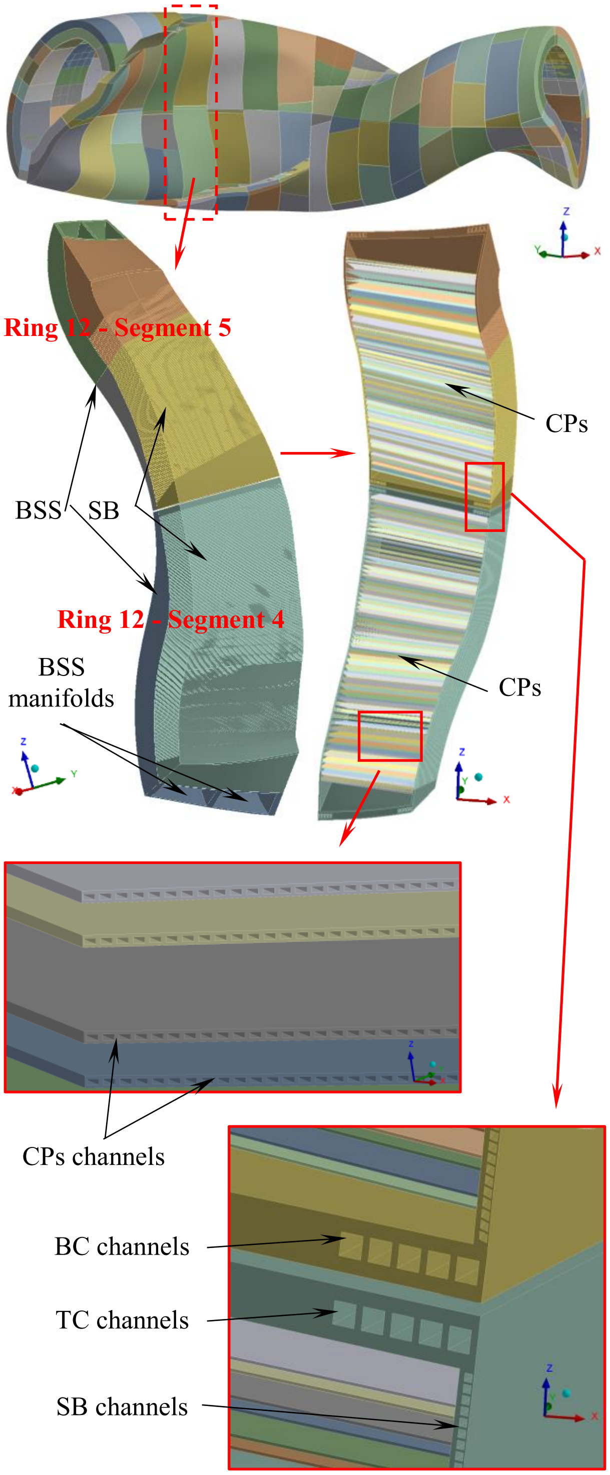

Fig. 10. Ring 12 segment 4 and segment 5 design.

Summarizing, the main features of the so designed segments are reported in Table 12.

Table 12. Number of components designed.

	Segment 4	Segment 5
SB channels	230	153
Caps channels (per cap)	5	5
CPs	110	92
CPs channels (avg. per cap)	68.6	69.7

4.2 The FEM model

As said above, the so designed Sgement 4 and Segment 5 of the Ring 12 HCPB BB have replaced the corresponding dummies within the HELIAS 5-B HCPB BB sector. Then, structural analysis have been performed under the over-pressurization loading scenario. It represents the limit conditions the BB segments may be undergone when an in-box Loss of Coolant Accident (in-box LOCA) occurs [30].

To this purpose, Segment 4 and Segment 5's SBs, CPs and BSSs have been assumed at 500 °C, which is considered as the limit operational temperature for the Eurofer steel. In addition, the HCPB BB design pressure of 9.2 MPa (namely the helium operational pressure of 8.0 MPa increased by a factor 1.15) has been imposed onto the SB internal surfaces not in contact with CPs (FW and SWs internals, CPs upper and lower surfaces, BSS) as well as within cooling channels (i. e. SB, CPs and Caps channels) and BSS manifolds.

As to the rest of the sector, the MCH loading conditions (reported in section 3.1) have been kept.

4.3 Results

Structural analysis of Segment 4 and Segment 5 of Ring 12 HCPB BB under over-pressurization conditions have been performed. The spatial distribution of the Von Mises equivalent stress arising within SBs is depicted in Fig. 11. From the reported contour maps, it is possible to see that the most of the investigated SBs domain experiences Von Mises stress quite lower than 350 MPa. Higher values are calculated within some regions of SWs and Caps.

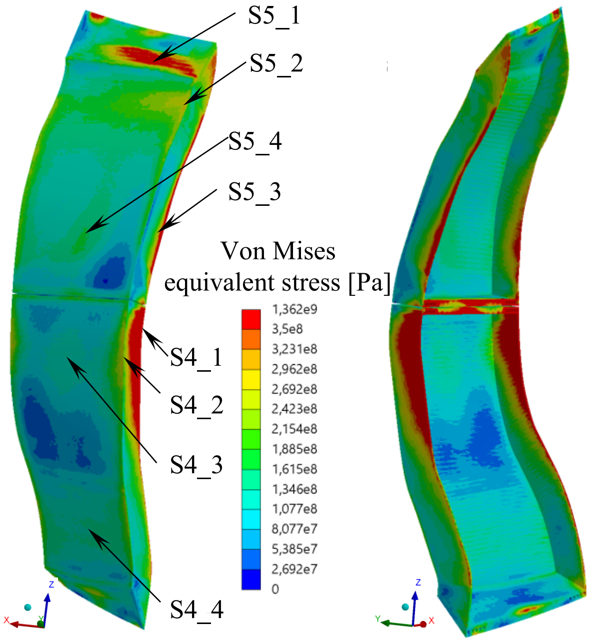

Fig. 11. SB Von Mises equivalent stress (primary + secondary loads) under over-pressurization conditions with indication of path locations.

Moreover, a stress linearization procedure has been performed in order to verify the fulfilment of the RCC-MRx structural design criteria in the most critical SB regions. As the considered scenario represents a severe accident, RCC-MRx the fulfilment of Level D criteria [31] has been checked. To this purpose, proper stress lines (paths) have been obtained through the FW, SWs and Caps thicknesses in those regions showing the highest Von Mises stress values. The identified path locations are indicated in Fig. 11 too.

Results of the RCC-MRx criteria verification are reported in Table 13 for segment 4 SB and in Table 14 for segment 5 SB. As it can be seen from the tables, the most of the criteria are fulfilled with a wide margin even in the most stressed regions.

Table 13. RCC-MRx Level D criteria verification for SB 4

Criterion	**S4_1**	**S4_2**	**S4_3**	**S4_4**
P_m / S_m	0.39	0.14	0.22	0.33
$(P_m + P_b) / (k_{eff} \cdot S_m)$	0.31	0.11	0.16	0.23
$(P_m + Q_m) / S_{em}$	1.51	0.41	0.23	0.22
$(P_m + P_b + Q + F) / S_{et}$	0.24	0.06	0.04	0.04

Table 14. RCC-MRx Level D criteria verification for SB 5

Criterion	**S5_1**	**S5_2**	**S5_3**	**S5_4**
P_m / S_m	0.30	0.45	1.75	1.34
$(P_m + P_b) / (k_{eff} \cdot S_m)$	0.48	0.31	1.29	1.02
$(P_m + Q_m) / S_{em}$	0.18	0.36	0.87	0.29
$(P_m + P_b + Q + F) / S_{et}$	0.09	0.07	0.15	0.05

In addition, the Von Mises equivalent stress field within BSSs and CPs is reported in Fig. 12 and Fig. 13 respectively.

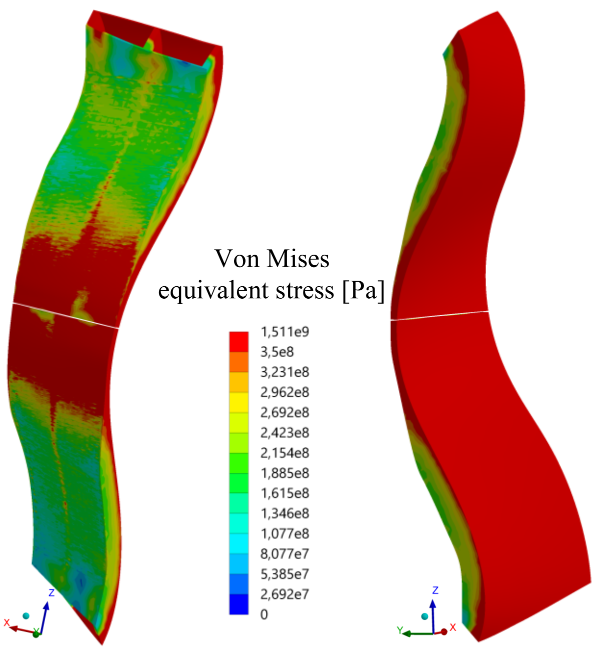

Fig. 12. BSS Von Mises equivalent stress (primary + secondary loads) under over-pressurization conditions.

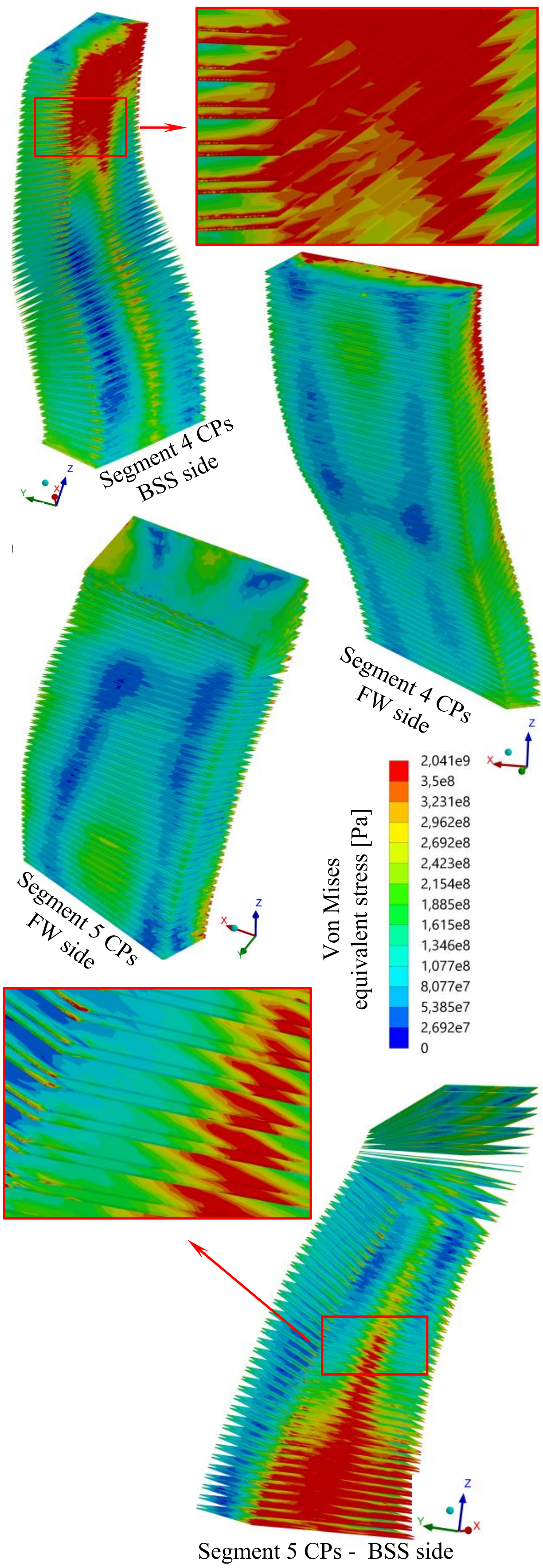

Fig. 13. CPs Von Mises equivalent stress (primary + secondary loads) under over-pressurization conditions.

The most of the BSS and CPs domains experience Von Mises equivalent stress lower than 350 MPa. In particular, the stress field within BSS strongly depends on the connection to VV and on its temperature. In this study, BSSs at 500 °C directly tied to a colder VV probably leads to a large over estimation of the actual Von Mises stress field within BSSs.

In conclusion, one can state that the obtained results are encouraging, suggesting further assessing the inboard segments of the Ring 12 HCPB BB with more detailed analysis. Firstly, different spatial arrangements of CPs and FW channels could be investigated in order to check the potentiality of each proposed design solution. Then, the best design options may be assessed under the over-pressurization conditions with non-uniform temperature distribution, once the neutronic data in terms of nuclear power spatial distribution will be available and the fully HELIAS-relevant thermal field will be calculated.

5. Conclusion

A structural assessment of a whole toroidal sector of the HELIAS 5-B breeding blanket, extending for 72° along toroidal direction, has been presented in this work.

In the first part, both HCPB and WCLL BB concepts have been considered in order to verify the feasibility of the proposed segmentation strategy for the whole sector. A totally heterogeneous model has been adopted for the BB segments and the VV. The obtained results in terms of displacements have allowed concluding that, in case of Hot VV conditions, overlapping between adjacent BB rings and/or segments can be excluded with a reasonable margin of confidence. In case of Cold VV, a proper attachment system will have to mechanically compensate the huge difference in temperature between VV and BB. In the second part, a detailed design of the inboard segments of a bean shape BB ring (Ring 12), conceived according the HCPB BB "sandwich" architecture, has been presented and assessed under severe accidental conditions. The detailed segments have replaced the corresponding dummies within the BB sector. The obtained results in terms of Von Mises stress field and RCC-MRx criteria verification have been promising, suggesting the follow-up of this assessment. The possible next steps might be the introduction of more realistic loading conditions (once necessary neutronic data will be available) together with the investigation of alternative design solutions for the BB components. Then, systems engineering approach may be also adopted to develop the HELIAS 5-B BB in a holistic way [32][33] and/or to decide the best concept to base on [34].

Acknowledgment

This work has been carried out within the framework of the EUROfusion Consortium and has received funding from the Euratom research and training programme 2014-2018 and 2019-2020 under grant agreement No 633053. The views and opinions expressed herein do not necessarily reflect those of the European Commission.

Appendix

The complete set of results in terms of minimum residual gaps, obtained in the first part of the study, is reported in this Appendix. As already seen for Ring 5 and Ring 12, both poloidal and toroidal overlapping can be excluded with a reasonable margin of confidence for Hot VV conditions also in the remaining 14 BB rings. In this case, narrow residual gaps (i. e. lower than 5 mm) are still predicted in specific locations. In case of Cold VV, proper attachments devoted to connect mechanically the VV to the BB should be able to compensate the high difference in thermal expansion between the systems, which presently causes overlapping.

Table 15. Minimum residual toroidal gaps - LC scenarios (E=10%).

Minimum residual toroidal gap						
	HCPB [mm]		WCLL [mm]		$\Delta_{LCC-LCH}$%	
Rings	LCC	LCH	LCC	LCH	HCPB	WCLL
1-2	8.3	10.8	11.9	15.5	31	31
2-3	4.4	10.6	10.8	15.7	143	45
3-4	3.0	9.9	8.4	15.3	230	83
6-7	4.8	10.8	9.7	15.8	126	62
7-8	7.6	10.3	11.5	15.3	36	33
8-9	4.7	11.1	9.4	15.8	137	68
9-10	5.6	11.6	10.1	16.0	105	58
10-11	5.6	11.5	10.1	15.9	105	58
13-14	7.5	12.7	11.4	16.6	70	45
14-15	5.8	11.6	10.2	16.0	101	57
15-16	5.3	11.4	9.8	15.9	115	62

Table 16. Minimum residual toroidal gaps - MC scenarios (E=100%).

Minimum residual toroidal gap						
	HCPB [mm]		WCLL [mm]		$\Delta_{MCC-MCH}$%	
Rings	MCC	MCH	MCC	MCH	HCPB	WCLL
1-2	4.2	12.0	11.8	15.4	187	30
2-3	5.0	9.9	10.3	15.5	101	51
3-4	3.7	9.3	9.7	15.3	152	58
6-7	5.7	10.6	11.0	15.9	85	44
7-8	8.2	9.8	12.2	15.2	20	24
8-9	5.5	10.7	10.5	15.7	96	50
9-10	8.9	12.6	13.8	16.7	42	21
10-11	5.9	10.9	10.8	15.8	85	46
13-14	8.6	12.6	12.7	16.6	47	31
14-15	6.4	11.2	11.1	15.9	77	44
15-16	6.4	11.3	13.8	17.0	75	24

Table 17. Ring 1 results - LC scenarios (E=10%).

Minimum residual poloidal gap						
	HCPB [mm]		WCLL [mm]		$\Delta_{LCC-LCH}$%	
Segment	LCC	LCH	LCC	LCH	HCPB	WCLL
1-2	0.1	8.9	5.9	14.7	6170	151
2-3	-0.3	8.2	5.6	14.2	2845	152
3-4	7.1	12.6	11.3	16.7	76	48
4-5	-5.5	5.8	1.6	13.0	206	699
5-1	-6.4	4.8	1.4	12.7	174	811

Table 18. Ring 1 results - MC scenarios (E=100%).

Minimum residual poloidal gap						
	HCPB [mm]		WCLL [mm]		$\Delta_{MCC-MCH}$%	
Segment	MCC	MCH	MCC	MCH	HCPB	WCLL
1-2	1.9	8.3	8.2	14.5	341	78
2-3	-1.6	6.0	5.8	13.4	478	133
3-4	9.8	13.4	13.5	17.1	37	27
4-5	-5.3	3.5	3.4	12.3	166	260
5-1	-4.1	4.3	4.3	12.7	206	194

Table 19. Ring 2 results - LC scenarios (E=10%).

Minimum residual poloidal gap						
	HCPB [mm]		WCLL [mm]		$\Delta_{LCC-LCH}$%	
Segment	LCC	LCH	LCC	LCH	HCPB	WCLL
1-2	-1.5	7.8	4.9	14.1	633	191
2-3	8.2	13.1	11.3	15.4	59	37
3-4	-3.9	5.9	3.2	13.1	253	310
4-5	4.7	11.1	9.9	16.0	137	62
5-1	-3.9	6.4	3.0	13.4	264	342

Table 20. Ring 2 results - MC scenarios (E=100%).

Minimum residual poloidal gap						
	HCPB [mm]		WCLL [mm]		$\Delta_{MCC-MCH}$%	
Segment	MCC	MCH	MCC	MCH	HCPB	WCLL
1-2	1.3	8.0	7.7	14.4	526	87
2-3	7.1	10.3	8.8	15.4	45	76
3-4	-5.1	3.5	3.6	12.2	169	239
4-5	8.6	12.2	12.9	16.6	42	29
5-1	-3.1	4.9	4.9	12.9	259	164

Table 21. Ring 3 results - LC scenarios (E=10%).

Minimum residual poloidal gap						
	HCPB [mm]		WCLL [mm]		$\Delta_{LCC-LCH}$%	
Segment	LCC	LCH	LCC	LCH	HCPB	WCLL
1-2	-1.2	8.0	6.8	14.3	797	108
2-3	0.9	8.8	8.6	14.7	873	71
3-4	3.2	9.9	5.1	15.3	208	199
4-5	-1.1	7.9	9.2	14.2	805	54
5-1	4.8	11.4	5.0	15.8	139	217

Table 22. Ring 3 results - MC scenarios (E=100%).

Minimum residual poloidal gap						
	HCPB [mm]		WCLL [mm]		$\Delta_{MCC-MCH}$%	
Segment	MCC	MCH	MCC	MCH	HCPB	WCLL
1-2	0.2	7.1	7.1	14.0	3071	98
2-3	4.5	9.7	10.1	15.3	118	52
3-4	7.1	11.2	12.0	16.1	58	34
4-5	-1.0	6.4	6.2	13.7	718	120
5-1	8.7	12.6	12.9	16.6	45	29

Table 23. Ring 4 results - LC scenarios (E=10%).

Minimum residual poloidal gap						
	HCPB [mm]		WCLL [mm]		$\Delta_{LCC-LCH}$%	
Segment	LCC	LCH	LCC	LCH	HCPB	WCLL
1-2	6.4	12.1	10.6	16.1	88	52
2-3	-4.3	5.9	3.3	13.4	237	306
3-4	8.0	13.1	11.6	16.7	63	43
4-5	-4.3	5.9	2.8	13.2	238	373
5-1	3.0	10.3	8.4	15.6	242	85

Table 24. Ring 4 results - MC scenarios (E=100%).

Minimum residual poloidal gap						
	HCPB [mm]		WCLL [mm]		$\Delta_{MCC-MCH}$%	
Segment	MCC	MCH	MCC	MCH	HCPB	WCLL
1-2	9.4	13.0	13.3	16.7	38	25
2-3	-2.7	5.0	5.5	13.3	284	141
3-4	10.1	13.6	13.6	17.1	35	25
4-5	-2.9	5.0	5.1	13.1	271	157
5-1	6.4	11.0	11.6	16.1	72	39

Table 25. Ring 6 results - LC scenarios (E=10%).

Minimum residual poloidal gap						
	HCPB [mm]		WCLL [mm]		$\Delta_{LCC-LCH}$%	
Segment	LCC	LCH	LCC	LCH	HCPB	WCLL
1-2	2.4	10.2	7.6	15.4	325	103
2-3	-3.0	6.9	0.0	13.7	328	-
3-4	4.3	11.1	9.0	15.9	158	76
4-5	-0.2	8.5	5.9	14.6	5027	147
5-1	5.8	11.8	10.1	16.2	104	59

Table 26. Ring 6 results - MC scenarios (E=100%).

Minimum residual poloidal gap						
	HCPB [mm]		WCLL [mm]		$\Delta_{MCC-MCH}$%	
Segment	MCC	MCH	MCC	MCH	HCPB	WCLL
1-2	5.6	10.6	10.7	15.8	90	47
2-3	-2.0	5.9	5.6	13.5	394	141
3-4	7.1	11.4	12.0	16.3	61	36
4-5	2.6	8.7	8.9	15.1	239	69
5-1	8.6	12.5	12.8	16.6	45	30

Table 27. Ring 7 results - LC scenarios (E=10%).

Minimum residual poloidal gap						
	HCPB [mm]		WCLL [mm]		$\Delta_{LCC-LCH}$%	
Segment	LCC	LCH	LCC	LCH	HCPB	WCLL
1-2	3.6	10.8	8.5	15.7	197	85
2-3	5.7	11.5	10.0	16.0	104	59
3-4	-4.1	5.8	3.1	13.2	240	320
4-5	-1.6	7.1	2.1	11.0	547	412
5-1	-5.0	5.9	2.1	13.1	219	511

Table 28. Ring 7 results - MC scenarios (E=100%).

Minimum residual poloidal gap						
	HCPB [mm]		WCLL [mm]		$\Delta_{MCC-MCH}$%	
Segment	MCC	MCH	MCC	MCH	HCPB	WCLL
1-2	6.5	11.2	11.3	16.0	73	42
2-3	9.2	12.7	13.2	16.7	38	26
3-4	-3.9	4.4	4.4	12.7	213	186
4-5	0.0	6.8	4.1	11.1	68k	170
5-1	-3.2	5.1	4.7	13.0	259	178

Table 29. Ring 8 results - LC scenarios (E=10%).

Minimum residual poloidal gap						
	HCPB [mm]		WCLL [mm]		$\Delta_{LCC-LCH}$%	
Segment	LCC	LCH	LCC	LCH	HCPB	WCLL
1-2	-6.9	4.6	0.8	12.5	167	1398
2-3	6.6	12.4	10.6	16.4	89	55
3-4	9.5	13.8	12.7	17.0	46	34
4-5	2.4	9.7	7.8	15.1	307	94
5-1	0.6	9.1	6.3	14.7	1377	134

Table 30. Ring 8 results - MC scenarios (E=100%).

Minimum residual poloidal gap						
	HCPB [mm]		WCLL [mm]		$\Delta_{MCC-MCH}$%	
Segment	MCC	MCH	MCC	MCH	HCPB	WCLL
1-2	-6.9	3.4	3.3	12.2	150	277
2-3	6.6	13.4	13.6	17.0	104	25
3-4	9.5	15.0	15.2	17.7	58	16
4-5	2.4	8.8	8.8	14.8	271	69
5-1	0.6	8.7	9.0	14.9	1317	66

Table 31. Ring 9 results - LC scenarios (E=10%).

Minimum residual poloidal gap						
	HCPB [mm]		WCLL [mm]		$\Delta_{LCC-LCH}$%	
Segment	LCC	LCH	LCC	LCH	HCPB	WCLL
1-2	-2.6	6.9	4.1	13.7	364	237
2-3	0.9	9.0	6.6	14.8	960	125
4-5	-1.4	7.6	5.1	14.1	639	177

Table 32. Ring 9 results - MC scenarios (E=100%).

Minimum residual poloidal gap						
	HCPB [mm]		WCLL [mm]		$\Delta_{MCC-MCH}$%	
Segment	MCC	MCH	MCC	MCH	HCPB	WCLL
1-2	-1.2	6.2	6.2	13.6	613	120
2-3	3.4	9.2	9.2	15.0	171	64
4-5	-0.2	7.1	6.7	14.1	3979	109

Table 33. Ring 10 results - LC scenarios (E=10%).

Minimum residual poloidal gap						
	HCPB [mm]		WCLL [mm]		$\Delta_{LCC-LCH}$%	
Segment	LCC	LCH	LCC	LCH	HCPB	WCLL
1-2	-2.6	7.1	4.0	13.8	370	243
2-3	-1.7	7.5	4.8	14.0	543	193
4-5	-2.2	6.8	4.6	13.7	406	199

Table 34. Ring 10 results - MC scenarios (E=100%).

Minimum residual poloidal gap						
	HCPB [mm]		WCLL [mm]		$\Delta_{MCC-MCH}$%	
Segment	MCC	MCH	MCC	MCH	HCPB	WCLL
1-2	-1.5	6.1	5.9	13.5	518	129
2-3	1.0	7.5	7.8	14.2	634	84
4-5	-1.9	5.9	5.7	13.5	418	136

Table 35. Ring 11 results - LC scenarios (E=10%).

Minimum residual poloidal gap						
	HCPB [mm]		WCLL [mm]		$\Delta_{LCC-LCH}$%	
Segment	LCC	LCH	LCC	LCH	HCPB	WCLL
1-2	0.0	8.5	6.0	14.6	121k	142
2-3	-5.4	5.3	2.0	12.9	198	536
4-5	-0.4	8.1	5.8	14.4	2198	149

Table 36. Ring 11 results - MC scenarios (E=100%).

Minimum residual poloidal gap						
	HCPB [mm]		WCLL [mm]		$\Delta_{MCC-MCH}$%	
Segment	MCC	MCH	MCC	MCH	HCPB	WCLL
1-2	1.6	8.0	8.1	14.6	411	79
2-3	-4.4	4.0	4.2	12.7	191	200
4-5	-1.1	6.5	6.2	13.9	676	125

Table 37. Ring 13 results - LC scenarios (E=10%).

Minimum residual poloidal gap						
	HCPB [mm]		WCLL [mm]		$\Delta_{LCC-LCH}$%	
Segment	LCC	LCH	LCC	LCH	HCPB	WCLL
1-2	-5.8	5.3	1.8	13.0	191	623
2-3	-3.5	6.4	3.4	13.5	283	301
4-5	1.9	9.8	7.2	15.2	424	111

Table 38. Ring 13 results - MC scenarios (E=100%).

Minimum residual poloidal gap						
	HCPB [mm]		WCLL [mm]		$\Delta_{MCC-MCH}$%	
Segment	MCC	MCH	MCC	MCH	HCPB	WCLL
1-2	-4.6	3.9	4.1	12.6	185	211
2-3	-2.1	5.6	5.7	13.4	370	134
4-5	2.0	8.9	8.0	14.9	341	86

Table 39. Ring 14 results - LC scenarios (E=10%).

Minimum residual poloidal gap						
	HCPB [mm]		WCLL [mm]		$\Delta_{LCC-LCH}$%	
Segment	LCC	LCH	LCC	LCH	HCPB	WCLL
1-2	-4.5	5.9	2.7	13.2	230	384
2-3	0.4	8.7	6.4	14.6	2281	129
4-5	0.6	8.9	6.5	14.9	1489	129

Table 40. Ring 14 results - MC scenarios (E=100%).

Minimum residual poloidal gap						
	HCPB [mm]		WCLL [mm]		$\Delta_{MCC-MCH}$%	
Segment	MCC	MCH	MCC	MCH	HCPB	WCLL
1-2	-2.9	5.1	5.1	13.1	278	158
2-3	2.3	8.5	8.6	14.7	273	72
4-5	0.3	7.5	7.1	14.3	2409	102

Table 41. Ring 15 results - LC scenarios (E=10%).

Minimum residual poloidal gap						
	HCPB [mm]		WCLL [mm]		$\Delta_{LCC-LCH}$%	
Segment	LCC	LCH	LCC	LCH	HCPB	WCLL
1-2	-2.0	7.3	4.7	14.0	475	198
2-3	-5.3	5.6	1.9	12.9	205	573
4-5	-0.7	7.9	5.8	14.5	1213	150

Table 42. Ring 15 results - MC scenarios (E=100%).

Minimum residual poloidal gap						
	HCPB [mm]		WCLL [mm]		$\Delta_{MCC-MCH}$%	
Segment	MCC	MCH	MCC	MCH	HCPB	WCLL
1-2	0.0	6.9	7.2	14.0	41k	95
2-3	-4.6	4.2	3.7	12.6	190	238
4-5	-0.2	6.9	7.0	14.0	4341	102

Table 43. Ring 16 results - LC scenarios (E=10%).

Minimum residual poloidal gap						
	HCPB [mm]		WCLL [mm]		$\Delta_{LCC-LCH}$%	
Segment	LCC	LCH	LCC	LCH	HCPB	WCLL
1-2	-2.1	7.3	4.5	14.0	443	209
2-3	-6.3	4.9	1.2	12.6	178	913
4-5	-2.0	7.4	4.7	14.1	465	201

Table 44. Ring 16 results - MC scenarios (E=100%).

	Minimum residual poloidal gap					
	HCPB [mm]		WCLL [mm]		$\Delta_{MCC-MCH}$%	
Segment	MCC	MCH	MCC	MCH	HCPB	WCLL
1-2	-0.2	6.7	7.0	13.9	3637	98
2-3	-5.7	3.4	3.0	12.2	160	307
4-5	-0.3	6.9	6.8	14.0	2395	106

References

[1] T. Donné et al., European Research Roadmap to the Realisation of Fusion Energy, EUROfusion, 2018 (ISBN 978-3-00-061152-0).

[2] F. Warmer et al., From W7-X to a HELIAS fusion power plant: On engineering considerations for next-step stellarator devices, Fus. Eng. Des. 123 (2017) 47-53.

[3] T. Klinger et al., Overview of first Wendelstein 7-X high-performance operation, Nucl. Fusion 59 (2019), 112004

[4] F. Schauer et al., HELIAS 5-B magnet system structure and maintenance concept, Fus. Eng. Des. 88 (2013) 1619-1622.

[5] U. Fischer et al., Nuclear design issues of a stellarator fusion power plant with breeder blanket in comparison to tokamaks, paper presented at 27th IAEA Fusion Energy Conference (FEC 2018).

[6] G. Bongiovì et al., Preliminary structural assessment of the HELIAS 5-B breeding blanket, Fus. Eng. Des., 146, pp. 55-58, 2019.

[7] G. Bongioví, A. Häußler, Progresses in the structural assessment of the central region of a HELIAS 5-B breeding blanket half sector, Fus. Eng. Des., 159, 111620, 2020.

[8] G. Bongioví, A. Häußler, Advancements in the HELIAS 5-B breeding blanket structural analysis, Fus. Eng. Des., 161, 111928, 2020.

[9] A. Häußler, Computational approaches for nuclear design analyses of the stellarator power reactor HELIAS, PhD thesis, DOI: 10.5445/IR/1000124072, 2020.

[10] G. A. Spagnuolo et al., Development of load specifications for the design of the breeding blanket system, Fus. Eng. Des., 157, 111657, 2020.

[11] G. Bongiovì et al., Multi-Module vs. Single-Module concept: Comparison of thermomechanical performances for the DEMO Water-Cooled Lithium Lead breeding blanket, Fus. Eng. Des., 2018, 136 Part B, pp. 1472-1478.

[12] G. A. Spagnuolo, EFDA_D_2N5LUV v1.0 - Blanket Material Composition For Neutronics - January2017, IDM document ref. 2N5LUV.

[13] F. Hernández et al., A new HCPB breeding blanket for the EU DEMO: Evolution, rationale and preliminary performances, Fus. Eng. Des. 124 (2017) 882-886.

[14] F. Hernández et al., Overview of the HCPB Research Activities in EUROfusion, IEEE Trans. on Pl. Sc. 46 (2018) 2247-2261.

[15] F. Hernández et al., Advancements in the Helium-Cooled Pebble Bed Breeding Blanket for the EU DEMO: Holistic Design Approach and Lessons Learned, Fusion Science and Technology, 75(5), pp. 352-364, 2019.

[16] E. Martelli et al., Advancements in DEMO WCLL breeding blanket design and integration, Int. J. Energy Res., 2018, 42; pp. 27-52.

[17] A. Tassone et al., Recent Progress in the WCLL Breeding Blanket Design for the DEMO Fusion Reactor, IEEE Trans. on Pl. Sc., 2018, 46, pp. 1446-1457.

[18] A. Del Nevo et al., Recent progress in developing a feasible and integrated conceptual design of the WCLL BB in EUROfusion project, Fus. Eng. Des., 146, pp. 1805-1809, 2019.

[19] J. Aubert et al., Status of the EU DEMO HCLL breeding blanket design development, Fus. Eng. Des., 2018, 136, Part B, 1428-1432.

[20] D. Rapisarda et al., Conceptual Design of the EU-DEMO Dual Coolant Lithium Lead Equatorial Module, IEEE Trans. on Pl. Sc., 2016, 44, pp. 1603-1612.

[21] P. A. Di Maio et al., Structural analysis of the back supporting structure of the DEMO WCLL outboard blanket, Fus. Eng. Des., 124, pp. 944-947, 2017.

[22] C. Bachmann, PDD-Plant Description Document v.1.3, https://idm.euro-fusion.org/?uid=2KVWQZ.

[23] C. Bachmann, PDD-Plant Description Document v.1.5, https://idm.euro-fusion.org/?uid=2KVWQZ.

[24] G. Zhou et al., Transient thermal analysis and structural assessment of an ex-vessel LOCA event on the EU DEMO HCPB breeding blanket and the attachment system, Fus. Eng. Des., 136, 34-41, 2018.

[25] P. A. Di Maio et al., On the thermo-mechanical behavior of DEMO water-cooled lithium lead equatorial outboard blanket module, Fus. Eng. Des. 124 (2017) 725-729.

[26] G. Federici et al., European DEMO design strategy and consequences for materials, Nucl. Fusion 57 (2017), 092002.

[27] P. Chiovaro et al., Assessment of the Thermo-mechanical Performances of a DEMO Water-Cooled Liquid Metal Blanket Module, J. Fusion Energ 34, 277-292 (2015), https://doi.org/10.1007/s10894-014-9789-z.

[28] A. Del Nevo et al., WCLL BB design and Integration studies 2019 activities, report on deliverable (https://idm.euro-fusion.org/?uid=2P5NE5).

[29] P. A. Di Maio et al., On the effect of stiffening plates configuration on the DEMO Water Cooled Lithium Lead Breeding Blanket module thermo-mechanical behavior, Fus. Eng. Des., 146 (2019), pp. 2247-2250.

[30] G. A. Spagnuolo et al., Development of load specifications for the design of the breeding blanket system, Fus. Eng. Des., 157, 111657, 2020.

[31] RCC-MRx, Design and Construction Rules for Mechanical Components of Nuclear Installations, AFCEN, 2013.

[32] G. Bongioví et al., Systems engineering activities supporting the heating & current drive and fuelling lines systems integration in the European DEMO breeding blanket, Fus. Eng Des., 2019, 147, 111265.

[33] G. A. Spagnuolo et al., Systems Engineering approach in support to the breeding blanket design, Fus. Eng. Des., 2019, 146, pp. 31-35.

[34] G. Bongioví et al., Concept selection of the automated inspection and maintenance test unit for the EU DEMO using a novel fuzzy-based decision support tool, Fus. Eng. Des., 2019, 148, 111324.